Journal of
Synchrotron
Radiation

ISSN 0909-0495

Received 25 July 2012
Accepted 2 January 2013

In situ synchrotron diffraction studies on the formation kinetics of jarosites

Nicola V. Y. Scarlett,[a]* Ian E. Grey[a] and Helen E. A. Brand[a,b,c]

[a]Process Science and Engineering, CSIRO, Box 312, Clayton South, Victoria 3169, Australia, [b]Bragg Institute, Building 87, ANSTO, Locked bag 2001, Kirrawee DC, NSW 2232, Australia, and [c]Australian Synchrotron, 800 Blackburn Road, Clayton, Victoria 3168, Australia. E-mail: nicola.scarlett@csiro.au

This paper reports the results of time-resolved synchrotron powder diffraction experiments where jarosites with different K/H_3O, K/Na and Na/H_3O ratios were synthesized *in situ* at temperatures of 353, 368 and 393 K in order to observe the effect on kinetics and species produced. The Na/H_3O sample formed monoclinic jarosite at all three temperatures, whereas the K/H_3O and K/Na samples formed as rhombohedral jarosites at 353 K, and as mixtures of rhombohedral and monoclinic jarosites at the higher temperatures. The relative amount of the monoclinic phase increased with increase in temperature. Unit-cell parameter changes with reaction time could be explained by changes in iron stoichiometry (samples become more stoichiometric with time) together with changes in K/H_3O and Na/H_3O ratios. The reaction kinetics have been fitted using a two-stage Avrami model, with two different Avrami exponents corresponding to initial two-dimensional growth followed by one-dimensional diffusion-controlled growth. Activation energies for the initial growth stage were calculated to be in the range 90–126 kJ mol^{-1}.

Keywords: jarosite; precipitation kinetics; time-resolved diffraction; powder X-ray diffraction synchrotron.

1. Introduction

Jarosites occur naturally and are also synthesized for a range of industrial and environmental applications. The formula for stoichiometric jarosite is $AFe_3(SO_4)_2(OH)_6$ where $A = K^+$, Na^+, H_3O^+, NH_4^+, Tl^+, $0.5Pb^{2+}$. The phases with $A = K^+$, Na^+ and H_3O^+ occur most commonly and correspond to the minerals jarosite, natrojarosite and hydroniumjarosite, respectively (Bayliss *et al.*, 2010). Jarosite compositions often differ significantly from the ideal formula, particularly when prepared at relatively low temperature (<413 K), both in having substitution of H_3O^+ for alkalis in the *A* cation site and by having a significant deficiency of iron, balanced by replacement of OH^- by H_2O (Basciano & Peterson, 2007; Dutrizac, 1983; Brown, 1970). In these non-stoichiometric jarosites, Nielsen *et al.* have also established *via* NMR the presence of H_2O on the *A* site (Nielsen *et al.*, 2008). Although jarosites are invariably described in the literature as having rhombohedral symmetry, $R\bar{3}m$, with $a_h \simeq 7.3$ Å, $c_h \simeq 17$ Å (Jambor, 1999), recent studies have shown that low-temperature syntheses can result in iron-deficient phases with monoclinic symmetry, $C2/m$ (Gasharova-Garbeva, 2000; Scarlett *et al.*, 2010). The lowering of symmetry is associated with ordering of iron-site vacancies (Grey *et al.*, 2011).

In bacterial bioleaching of sulfide ores, jarosite phases can form as surface layers that passivate the ore against further leaching. Current bioleaching studies in this laboratory have been hampered by such passivation by jarosites (Zeng *et al.*, 2011). The *in situ* powder X-ray diffraction study reported here was initiated in order to gain an understanding of the early stages of nucleation and growth of jarosites, in the expectation of being able to apply this knowledge to controlling jarosite formation during bioleaching. Samples with different *A* cations (Na^+/H_3O^+, K^+/H_3O^+ and K^+/Na^+) were synthesized from solution at temperatures of 353, 368 and 393 K, accompanied by the continuous collection of diffraction data. These experiments were conducted in parallel with a series of identical syntheses in which small-angle X-ray scattering (SAXS) data were collected throughout the duration of the synthesis (Brand *et al.*, 2012). The purpose of this combined experimentation was to collect data from the earliest point of nucleation (SAXS) and then throughout the crystallization process (XRD). Synchrotron radiation was used in order to obtain the best possible lower limits of detection and to capture the earliest stages of nucleation and crystallization. Preliminary crystallographic results for the Na^+/H_3O^+ jarosite have been reported (Scarlett *et al.*, 2010).

2. Experimental

2.1. Synthesis

This study considered the use of K or Na or a combination of both as the *A*-site cation in the jarosites formed here. In reality the *A* site contains a mixture of the cation and H_3O^+. In order to explore this further a series of different atomic ratios of $[Fe^{3+}]/[K^+]$ were also considered. Depending upon the experiment, 1.74 g of $Fe_2(SO_4)_3{\cdot}9H_2O$ and one of the cation choices listed below [designated (*a*), (*b*) or (*c*)] were dissolved in 10 ml of deionized water and filtered through a Millipore syringe filter to remove any undissolved particles which may act as nucleation sites:

(*a*) Na series: 0.57 g of Na_2SO_4;

(*b*) K series: 0.23 g (K1), 0.46 g (K2) or 0.70 g (K3) of K_2SO_4;

(*c*) KNa series: 0.35 g of K_2SO_4 plus 0.28 g of Na_2SO_4.

These weights gave approximate molar ratios of 4 Na:3 Fe or 1 K:3 Fe (K1) or 2.5 K:3 Fe (K2) or 4 K:3 Fe (K3) or 2 Na:2 K:3 Fe. A portion of the resultant solution was then syringed into a 1.0 mm quartz glass capillary reaction vessel. Note that results for the K3 member of the K series of experiments have been published previously (Brand *et al.*, 2012) and are only described briefly here for comparison.

2.2. Diffraction

Each solution-filled capillary was mounted in a purpose-built sample stage on a goniometer head and placed at the centre of the powder diffractometer at the Australian Synchrotron (Wallwork *et al.*, 2007). A wavelength of 0.9523 Å was employed. The detector at the synchrotron is a position-sensitive Mythen detector (Schmitt *et al.*, 2003) covering 80° in 2θ with an inherent resolution of 0.004° in 2θ. The detector has a series of modules, each covering 5°, with a 0.2° gap between each module. At each temperature, pairs of data sets were collected at two detector settings, 0.5° apart, and the data sets merged to remove the gaps resulting from the spacing between detector modules.

For the *in situ* runs, the capillaries were pressurized using nitrogen gas at up to 4 bar as required to prevent boiling of the solution, oscillated about their axes and heated with a hot-air blower. This experimental set-up has been described in detail previously (Madsen *et al.*, 2005; Norby *et al.*, 1998; Scarlett *et al.*, 2008). Continuous pairs of 30 s datasets were then collected at temperatures of 353, 368 and 393 K throughout the duration of the reactions or for as long as was practical given time constraints (2–8 h).

2.2.1. Rietveld refinment. The Rietveld refinements were conducted using the *TOPAS* software (Bruker AXS, 2009) to determine structural changes with time and rates of crystallization. The methodology for analysis of the *in situ* diffraction data has been described previously (Grey *et al.*, 2011; Scarlett *et al.*, 2010, 2011) and will thus be only briefly described here. The starting atomic coordinates for the *in situ* refinements were taken directly from Basciano (2008) for rhombohedral jarosite and from Scarlett *et al.* (2010) for monoclinic jarosite. These, along with atomic displacement (for all non-hydrogen atoms) and sample displacement parameters, were determined from the final dataset at the temperature for each experiment, fixed at the refined values and used subsequently in the batch refinements of the *in situ* synthesis data. It is acknowledged that some of these parameters may have been changing with time but the data quality (particularly during the earlier portions of the experiments where little crystalline material was apparent) precluded detailed refinement of all parameter values throughout the experiments. This approach was deemed to be a satisfactory approximation and examination of individual refinement results throughout each experiment confirmed this. The sample displacement parameters were necessary as the jarosite nucleated on the walls of the capillaries, creating, in effect, two samples displaced equally and opposite from one another across the centre of the diffractometer (Scarlett *et al.*, 2011). The *A*-site occupancies (K/H_3O or Na/H_3O) were obtained from chemical analyses on *ex situ* hydrothermal syntheses, run for similar times as the *in situ* runs. The batch processes refined the entire suite of data (up to 350 datasets) for each particular experiment sequentially and in reverse order with the scale, unit-cell parameters and site occupancy for Fe sites as the key refinement parameters. In some refinement runs, where single-phase jarosite was produced in sufficient quantity, the K/H_3O or Na/H_3O ratios in the *A* site were also allowed to vary. Peak shapes were modelled using a Thompson–Cox–Hastings pseudo-Voigt function (Thompson *et al.*, 1987) and the Stephens strain models as appropriate (Stephens, 1999). The values for these parameters were also established from the final dataset at temperature and then fixed for the subsequent refinement of the remainder of the suite. This gave, in effect, an empirical model for peak shape. The background undulations resulting from the capillary itself and the solution were modelled by the combination of five pseudo-Voigt peak functions.

The refined Rietveld scale parameters, *s*, were normalized to a constant beam current of 200 mA and used to calculate scaling parameters (SP) for each phase using equation (1),

$$\mathrm{SP} = sZMV, \tag{1}$$

where *M* is the formula weight of the phase, *Z* is the number of formula units per unit cell and *V* is the unit-cell volume. The use of equation (1) rather than the Rietveld scale factor alone puts the abundances of the monoclinic and rhombohedral phases, which have different unit-cell contents, on an equivalent scale.

3. Results and discussion

3.1. Crystal chemistry

With the exception of a study by Gasharova-Garbeva (2000), all previous published works on jarosites report their symmetry to be rhombohedral. The high resolution obtained in these synchrotron studies revealed small peak splittings consistent with a lowering of the symmetry to monoclinic, space group *C*2/*m* (Grey *et al.*, 2011; Scarlett *et al.*, 2011),

under some conditions. The monoclinic phases have unit-cell parameters related to those for the rhombohedral cell by the vector relations $\mathbf{a}_m = \mathbf{a}_h - \mathbf{b}_h \simeq 12.7$ Å, $\mathbf{b}_m = \mathbf{a}_h + \mathbf{b}_h \simeq 7.3$ Å, $\mathbf{c}_m = 1/3(-\mathbf{a}_h + \mathbf{b}_h + \mathbf{c}_h) \simeq 7.0$ Å, and with $\beta \simeq 126$–127°. The symmetry lowering is associated with an ordering of iron-site vacancies in one of two independent iron sites, resulting in a breaking of the two-dimensional kagomé nets of iron atoms into one-dimensional chains (Grey *et al.*, 2011).

In the *in situ* study reported here, all combinations of temperature and starting compositions considered produced jarosite phases only. The Na series of syntheses gave a single monoclinic phase at 353 and 368 K and a mixture of monoclinic and rhombohedral phases at 393 K. In contrast, the K-series members K1, K2 and K3 all produced a single rhombohedral jarosite at 353 K, and mixtures of rhombohedral and monoclinic jarosites at 368 and 393 K. The peak splitting from symmetry lowering is illustrated in Fig. 1 for the $(012)_h$ reflection, shown for rhombohedral, monoclinic and mixed rhombohedral/monoclinic phases.

The relative amounts of rhombohedral and monoclinic jarosites at the end of each synthesis run are given in Table 1. These are derived directly from the Rietveld refinement *via* the Hill & Howard (1987) algorithm for quantitative phase analysis based upon the ratio of the *sZMV* of each phase to the sum of *sZMV* of the mixture (where *s* is the Rietveld scale factor, *M* is the formula weight of the phase, *Z* is the number of formula units per unit cell and *V* is the unit-cell volume). The severe overlap between the monoclinic and rhombohedral phases makes this partitioning somewhat inaccurate and little significance may be given to these values. However, it appears that the relative proportion of the monoclinic phase generally increases with increasing temperature. The phase contents for the KNa series are similar to those for the K1/K2 syntheses, and are quite different to those for the Na series. This is not surprising, given the very strong K partitioning into jarosite precipitated from solutions containing both Na and K. From Dutrizac's (1983) study, a solution containing equal molar contents of Na and K (as for the KNa series here) gives a precipitated jarosite containing 92% K:8% Na. Similar proportions have been confirmed by chemical analysis of jarosite prepared by *ex situ* hydrothermal synthesis using the KNa series starting solution.

Table 1
Jarosite polymorphs produced at the temperatures considered here where R = rhombohedral, M = monoclinic.

As each reaction ran for a different total time, for comparison the 368 K quantifications are all given for ~300 min of reaction time and for the 393 K values ~48 min of reaction time.

	Phases produced		
Reaction	353 (K)	368 (K)	393 (K)
K1	R	R(62%) + M(38%)	R(62%) + M(38%)
K2	R	R(54%) + M(46%)	R(44%) + M(56%)
K3	R	R(62%) + M(38%)	R(54%) + M(46%)
KNa	R	R(56%) + M(44%)	R(50%) + M(50%)
Na	M	M	R(44%) + M(56%)

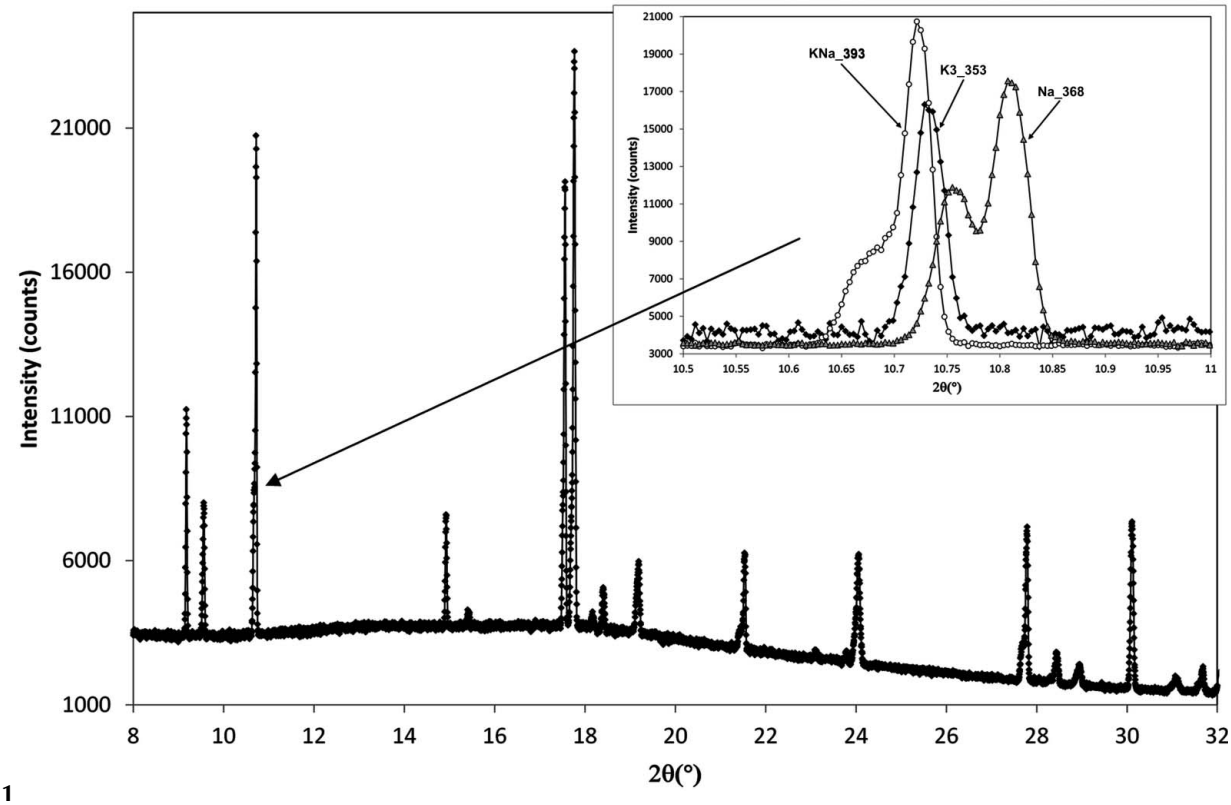

Figure 1
Synchrotron data set after KNa jarosite formation at 393 K. The inset shows magnification of the $(012)_h$ reflection for rhombohedral (K3_353), monoclinic (Na_368) and mixed rhombohedral/monoclinic (KNa_393) jarosite phases. (Note: the intensities of K3_353 and Na_368 are scaled arbitrarily for comparison.)

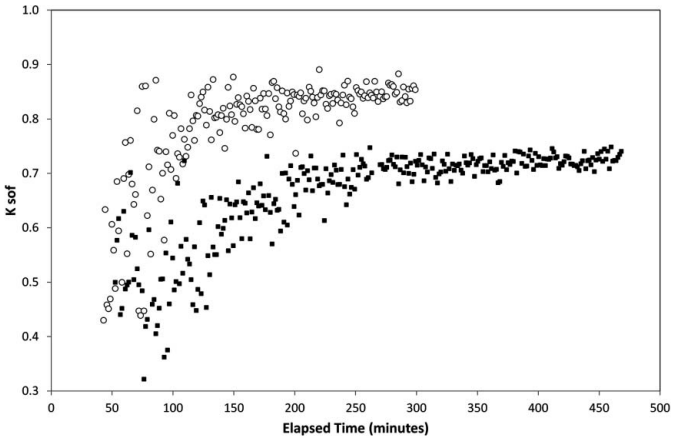

Figure 2
Variation of K-site occupancy with reaction time for K3 (white circles) and KNa (black squares); jarosite synthesis at 353 K.

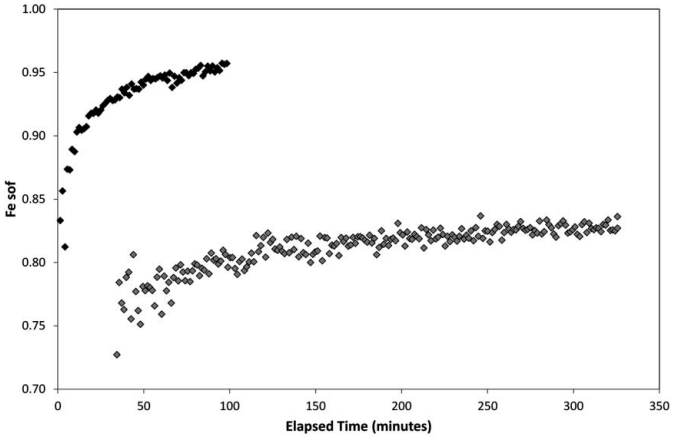

Figure 3
Variation of Fe-site occupancy with reaction time for synthesis of rhombohedral jarosite at 368 K and 393 K. Grey diamonds = KNa_368; black diamonds = KNa_393.

In principle, the compositional variations during the kinetic runs should be directly obtainable from site occupancy refinements of K/H_3O and Na/H_3O in the *A* site and Fe/vacancy refinements in the Fe sites. In practice, however, the weak diffraction patterns and high backgrounds from the solution resulted in considerable scatter of site occupancies in the *A* site, especially for Na/H_3O, where the scattering contrast is weak, and in the early stages of the reactions, where the diffraction peaks are barely above background. Consistent results were obtained for K/H_3O refinements for reactions which produced pure rhombohedral phases (K-jarosites, 353 K). All mixed phase reactions had the K-site occupancy fixed to values obtained from chemical analysis of equivalent jarosites prepared by *ex situ* hydrothermal synthesis. Fe-site occupancy refinements were stable for all K reactions once sufficient time had elapsed (after approximately 150 min at 353 K, 35 min at 368 K and 5 min at 393 K). With increasing time of reaction, there is a steady increase in K occupancy of the *A* sites and an increase in the Fe-site occupancy as shown by the examples in Figs. 2 and 3. It should be noted that even after extended reaction time the jarosites formed are non-

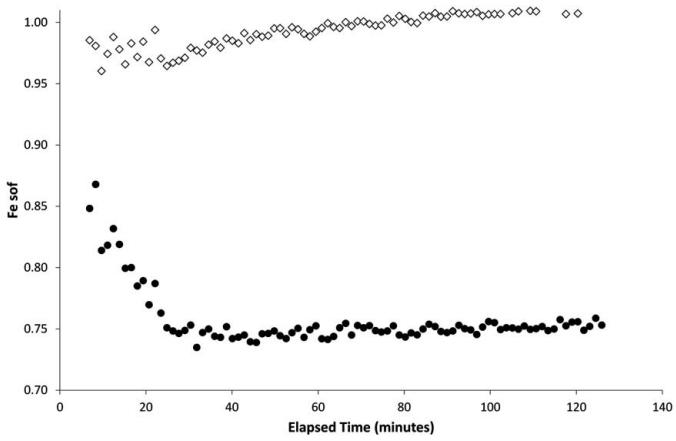

Figure 4
Variation of Fe-site occupancy with reaction time for synthesis of monoclinic natrojarosite at 393 K. Black circles = Fe1 Na393_M; white diamonds = Fe2 Na393_M.

stoichiometric. Previous work (Grey *et al.*, 2011) has shown consistent results with the model of Nielsen *et al.* (2008), who proposed the following charge-compensation mechanism for iron vacancies where four OH^- ions coordinated to iron are protonated to give four H_2O, with one of the protons coming from deprotonation of *A*-site H_3O^+. The formula for non-stoichiometric jarosite is thus

$$\left[A_{1-x}(H_3O)_{x-y}(H_2O)_y\right]Fe_{3-y}\left[(SO_4)_2(OH)_{6-4y}(H_2O)_{4y}\right].$$

As shown previously (Grey *et al.*, 2011; Scarlett *et al.*, 2011), in monoclinic jarosite there are two Fe sites and the Fe vacancies in non-stoichiometric monoclinic jarosite order preferentially into the Fe1 site (0, 0, 0.5). This is shown in Fig. 4 by the clear partitioning of the site occupation factors for Fe1 and Fe2 in the monoclinic Na jarosite synthesized at 393 K.

The most reliably determined parameters from the Rietveld refinements are the unit-cell parameters, and these can be used to infer crystal chemical changes during the kinetic runs. Plots are shown in Fig. 5 of the variation of hexagonal a_h *versus* c_h parameters during kinetic runs for the KNa-series syntheses. In the case of the monoclinic phases, the monoclinic cell parameters have been converted to pseudohexagonal (a_{ph} and c_{ph}) cell parameters using the relations

$$a_{ph} = \frac{1}{3}\left[(2a/\sqrt{3}) + b\right], \quad (2)$$

$$c_{ph} = (a^2 + 9c^2 + 6ac\cos\beta)^{1/2}. \quad (3)$$

This conversion allows a direct comparison of the results for both phases with the published results for near-stoichiometric rhombohedral K/H_3O jarosite solid solution phases (Basciano & Peterson, 2007). As seen from Fig. 5, the variations of a_h *versus* c_h with increasing reaction time are almost linear and are close to parallel to the line for the $KFe_3(SO_4)_2(OH)_6$–$(H_3O)Fe_3(SO_4)_2(OH)_6$ solid solution, for both the rhombohedral and monoclinic phases at the three temperatures. The progressive upward shift of the data plots with increasing synthesis temperature is consistent with the reported large

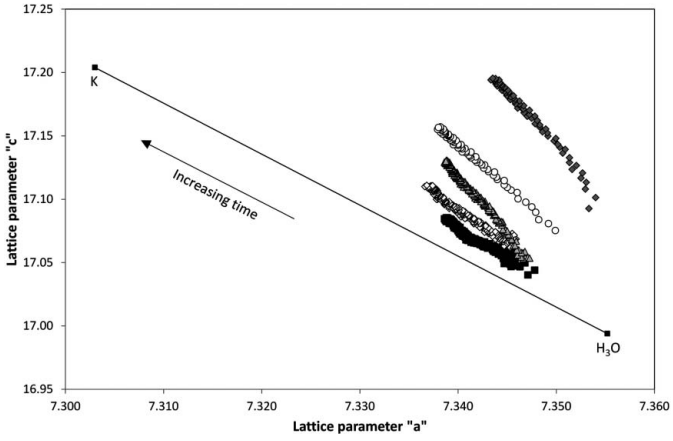

Figure 5
Variation of hexagonal cell parameters with time for the KNa series. Black squares = KNa_353; white diamonds = KNa_368_R; grey triangles = KNa_368_M; white circles = KNa_393_R; dark grey diamonds = KNa_393_M. The literature values of $(K_{0.368}H_3O_{0.05})Fe_3(SO_4)_2(OH)_6$–$H_3OFe_3(SO_4)_2(OH)_6$ (Basciano & Peterson, 2007) are shown as black filled squares joined by a solid line. Where monoclinic phases have formed, pseudo-hexagonal axes have been calculated.

thermal expansion of the c_h parameter for jarosite (Xu *et al.*, 2010). At 368 and 393 K, where rhombohedral and monoclinic phases co-exist, the data points for the monoclinic phase are displaced vertically relative to the points for the co-existing rhombohedral phase, corresponding to a larger equivalent rhombohedral volume of the monoclinic phase. Plots of a_h *versus* c_h for the different K-series rhombohedral phases formed at 368 K are compared in Fig. 6. The plots are progressively displaced vertically from K3 to K2 to K1, corresponding to increasing cell volumes in this order. The same relative offsets were obtained for the co-existing monoclinic phases. This is shown by plots of unit-cell volumes *versus* reaction time for the rhombohedral and monoclinic phases in Figs. 7(*a*) and 7(*b*), respectively. The changes in cell parameters and the increase in cell volume with reaction time

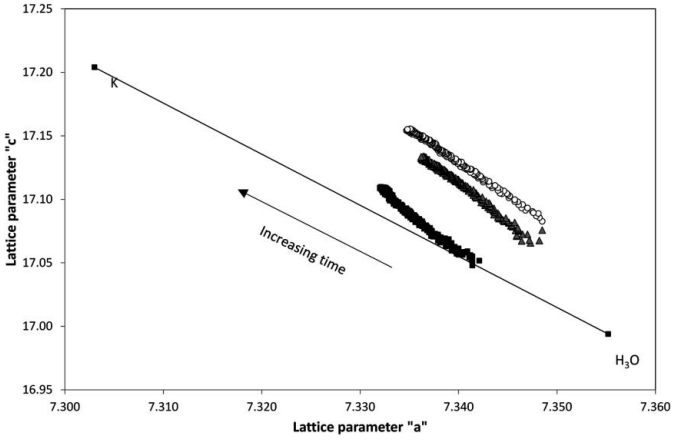

Figure 6
Variation of hexagonal cell parameters with time for the K-series rhombohedral phase syntheses at 368 K. Black squares = K3; grey triangles = K2; white circles = K1. The literature values of $(K_{0.368}H_3O_{0.05})Fe_3(SO_4)_2(OH)_6$–$H_3OFe_3(SO_4)_2(OH)_6$ (Basciano & Peterson, 2007) are shown as black filled squares joined by a solid line.

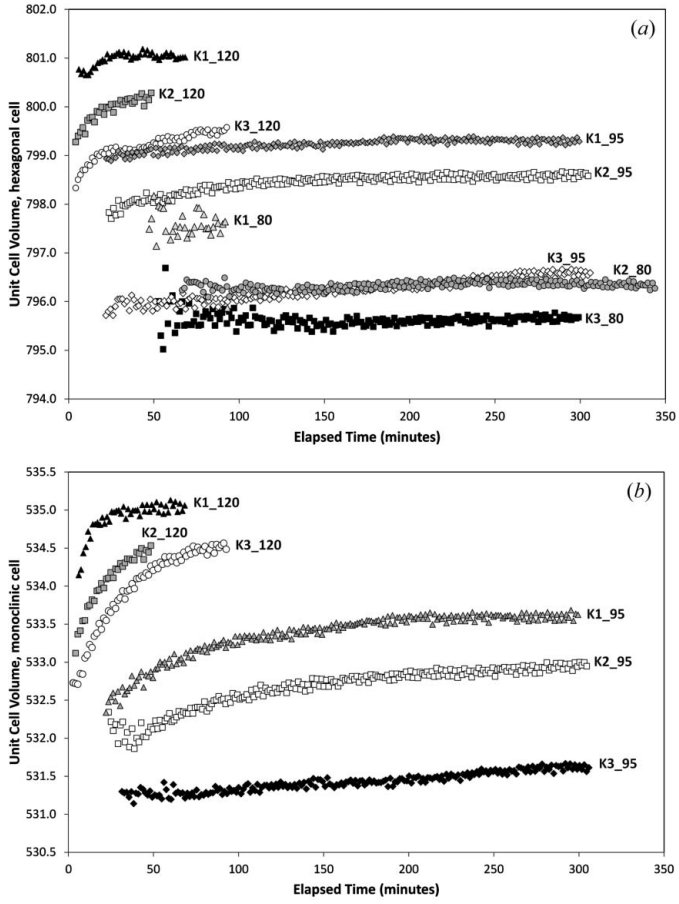

Figure 7
Unit-cell volumes as a function of reaction time for K-series (*a*) rhombohedral jarosites and (*b*) monoclinic jarosites.

for the K-series syntheses are consistent with initial compositions that are enriched in H_3O at the *A* site, and with a progressive replacement of H_3O by K as the jarosite crystals grow with time. Increasing K at the *A* site with reaction time was confirmed directly from site occupancy refinements as shown in Fig. 2. The progressive increase in Fe occupancy with increasing time (increasing stoichiometry), as shown in Fig. 3, will also contribute to an increase in the c_h parameter and the cell volume. Fig. 2 shows little difference in the K occupancy between K3 and K2 so the vertical offset between the data sets for K3 and K2, shown in Fig. 6, and the corresponding increase in volume from K3 to K2 (Fig. 7) cannot be explained solely by variations in K/H_3O at the *A* site. (Note that K1 also exhibits the same vertical offset in Fig. 6 and increasing volume in Fig. 7 but the corresponding K3-site refinement on the 353 K experiment was not possible as the reaction did not proceed for sufficient time.) The observed changes are therefore most likely due to increased occupancy of the Fe site from K3 to K2 to K1. Kubisz (1970) has previously noted that K/H_3O jarosites become progressively more stoichiometric when prepared from solutions with increasing [Fe]/[K] atomic ratio (as for K3 to K2 to K1). Basciano & Peterson (2007) have demonstrated that increased Fe contents of K/H_3O jarosites also results in increased unit-cell volumes (large effect on c_h, small on a_h).

The changes in crystal chemistry during growth of crystals of the Na series are quite different to those for the K-series members. The major difference is that for the Na-series solutions the jarosites formed at 353 and 368 K have pure monoclinic symmetry. In *ex situ* syntheses we have shown that rhombohedral Na/H_3O jarosites only form after extended reaction times at elevated ($\geq$393 K) temperatures (Grey *et al.*, 2011). The unit-cell changes with reaction time for the Na series differ significantly from those for the K series. Plots of pseudohexagonal a_{ph} *versus* c_{ph} cell parameter variations with reaction time for the Na series (Fig. 8) are not parallel to the line for the stoichiometric $NaFe_3(SO_4)_2(OH)_6$–$H_3OFe_3(SO_4)_2(OH)_6$ solid solution (Basciano, 2008), as found for the K series (Figs. 5 and 6).

The different cell parameter behaviour for Na and K series can be explained by different cell parameter responses to changing *A*-site occupation by Na/H_3O or K/H_3O on the one hand and changing Fe-site occupation on the other. For the K-series syntheses, increasing K and Fe content with reaction time both result in decreasing a_h and increasing c_h, so the two compositional effects are reinforced in the cell parameter changes. In contrast, for the Na-series syntheses, increasing Na content in the *A* site results in a decrease in both a_h and c_h whereas increasing Fe content gives a decrease in a_h and an increase in c_h so there is reinforcement of the changes in a_h but partial cancelling of the changes in c_h.

Fig. 8 shows the variation in the lattice parameters for the three different temperatures of natrojarosite synthesis. At 353 K the lattice parameters are fairly constant which is consistent with the slow rate of reaction. At 368 K the decrease in c_{ph} dominates the early part of the reaction indicating that the increase in Na content at the *A* site is dominating the growing crystals. However, what should be a corresponding decrease in a_{ph} may be being offset by an increase in the Fe vacancies in this early part of the reaction as the ordering of the Fe occurs (Fig. 4). This rate of decrease in c_{ph} slows with time and a very small decrease in a_{ph} is observed suggesting the reinforcement of the change in this parameter by a subsequent increase in the Fe content. This is consistent with the general trend in measured compositions of equivalent *ex situ* experiments (Table 2). The change in the lattice parameters at 393 K is somewhat different. For both the rhombohedral phase and the pseudo-hexagonal axes of the monoclinic phase there is a slight increase in c_{ph} early in the reaction accompanied by a significant decrease in a_{ph}. This suggests an early increase in Fe occupation followed by an increase in Na at the *A* site as observed for the 368 K reaction. It may be that the behaviour of the 368 K sample may come to follow the course of the 393 K sample given sufficient time and that the same early process as 368 K is occurring at 393 K but at too fast a rate for observation. Fig. 9 shows the overall decrease in unit-cell volume for all reactions consistent with the dominant replacement of H_3O by Na at the *A* site.

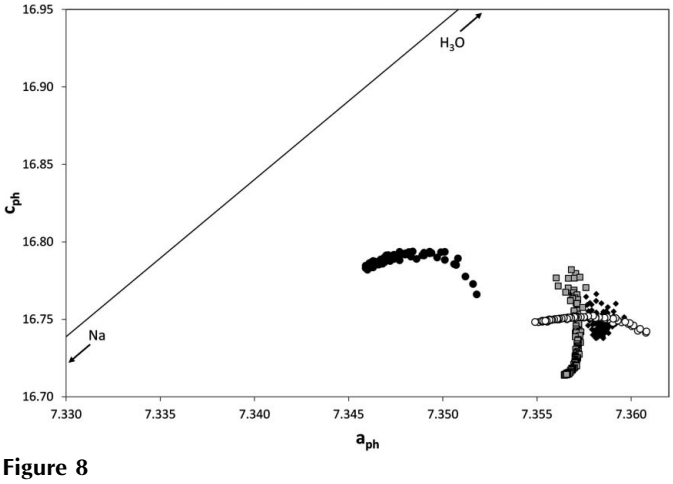

Figure 8
Variation of pseudohexagonal lattice parameters with time for formation of monoclinic jarosite in the Na series along with the lattice parameters from the minor rhombohedral phase formed at 393 K. The line corresponds to the stoichiometric solid solution $NaFe_3(SO_4)_2(OH)_6$–$H_3OFe_3(SO_4)_2(OH)_6$ (from Basciano & Peterson, 2008). Black diamonds = 353 K; grey squares = 368 K; white circles = 393 K, monoclinic; black circles = 393 K, rhombohedral.

Table 2
Analysis of products of *ex situ* syntheses conducted under the same conditions as the Na series reaction conducted at 368 K.

The values were obtained by ICP-OES and are given as oxide weight percentages along with the equivalent molar proportions.

Reaction time (h)	Na_2O	Fe_2O_3	SO_3	[Na]:[Fe]:[S]
2	4.3	45.8	34.2	0.65:2.68:2
4	4.5	45.3	34.2	0.67:2.66:2
5	4.5	47.5	34.1	0.68:2.79:2
42	4.2	47.3	33.3	0.65:2.85:2

3.2. Kinetics

Kinetic analysis of the SP values described above with respect to time has been conducted according to the methodology outlined by Brand *et al.* (2012). Briefly this has entailed the fitting to the data of a modified Avrami model proposed by Khanna & Taylor (1988) as shown in equation (4) below,

$$SP = SP_{max}\{1 - \exp[-(kt)^n]\}, \quad (4)$$

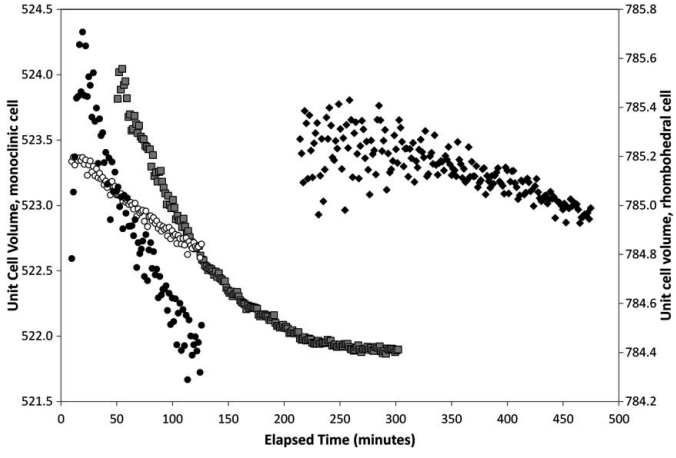

Figure 9
Variation of unit-cell volume as a function of reaction time for the Na series. Black diamonds = 353 K; grey squares = 368 K; white circles = 393 K, monoclinic; black circles = 393 K, rhombohedral.

Table 3
Fitted Avrami coefficients including fit residuals for modified Avrami expression for jarosite crystallization at 353, 368 and 393 K.

T (K)	k_1 (min^{-1})	t_0 (min)	n_1	Switch (min)	k_2 (min^{-1})	n_2	SP_{max}	χ^2
K1								
353	0.008 (5)	30 (0)†	1.7 (1)	N/A	N/A	N/A	6 (5)‡	0.044
368	0.0251 (4)	5.3 (3)	1.51 (3)	73.00 (3)	0.0058 (3)	0.71 (1)	29.1 (5)	0.033
393	0.143 (3)	4.51 (2)	1.29 (2)	17.89 (3)	0.0599 (4)	0.86 (2)	44.6 (2)	0.027
K2								
353	0.00473 (5)	30 (1)	1.55 (2)	N/A	N/A	N/A	10.7 (1)‡	0.033
368	0.0192 (2)	11.9 (3)	1.56 (2)	91.69 (3)	0.0066 (1)	0.92 (1)	29.0 (3)	0.028
393	0.112 (2)	1.56 (8)	1.56 (4)	15.27 (3)	0.0699 (6)	0.97 (3)	46.8 (3)	0.030
K3								
353	0.00416 (6)	19 (3)	2.05 (5)	N/A	N/A	N/A	9.1 (2)‡	0.032
368	0.0155 (4)	9.3 (3)	1.48 (3)	91.94 (3)	0.0062 (1)	1.02 (1)	31.9 (3)	0.031
393	0.116 (2)	0.78 (8)	1.59 (4)	16.34 (4)	0.0613 (6)	0.74 (2)	44.5 (2)	0.041
KNa								
353	0.0033 (1)	9 (3)	1.99 (5)	N/A	N/A	N/A	16.1 (5)‡	0.038
368	0.0180 (2)	7.1 (5)	1.86 (4)	87.68 (3)	0.0066 (1)	0.980 (9)	24.9 (1)	0.026
393	0.086 (1)	2.24 (5)	1.27 (2)	30.02 (5)	0.046 (1)	0.68 (4)	52.2 (8)	0.053
Na								
353	0.0007 (8)	108 (10)	2.2 (1)	N/A	N/A	N/A	47 (109)‡	0.025
368	0.0071 (1)	19 (1)	2.17 (4)	162.36 (2)	0.00447 (4)	1.91 (2)	18.7 (2)	0.018
393	0.0620 (9)	1.7 (2)	1.81 (5)	30.32 (4)	0.0359 (3)	0.90 (2)	33.3 (1)	0.042

† Fixed at observed value as insufficient data to determine reliably. ‡ Values quoted for first regime where switch point has not been reached.

where SP is the scaling parameter derived from the Rietveld refinement, SP_{max} is the maximum value of SP, k is the rate (min^{-1}), t is the elapsed time (min) and n is the Avrami exponent.

This has been achieved using a Monte Carlo approach implemented within the *TOPAS* software (Bruker AXS, 2009). *TOPAS* allows the inclusion of 'user-defined' macros in its code which meant that equation (4) could be readily applied to data comprising the elapsed time and SP determined from the traditional Rietveld refinement. Using this methodology two sequential kinetic models (designated Regime 1 and Regime 2) along with the switchover point between the two were refined over the full range of the data. Fig. 10 shows this graphically for Na at 368 K. The equations used were of the form given in equation (4) with the addition of a parameter (t_0) representing the induction period in minutes for the reaction in the first regime [equation (5)],

$$\mathrm{SP} = \mathrm{SP}_{max}\left(1 - \exp\left\{-\left[k(t - t_0)\right]^n\right\}\right). \quad (5)$$

The results of this modelling are given in Table 3 along with the calculated residuals for the fit.

It can be seen that in general the induction period declines with increasing temperature. With respect to composition there is little difference between K2 and K1 but the induction periods for KNa and K at 353 K are shorter. Na has a much longer induction period than any other composition at 353 K but is similar to the others at 368 K and 393 K.

None of the reactions described here proceeded to completion owing to time constraints regarding synchrotron data collection. However, all those conducted at 368 K and 393 K were best modelled using two different rate equations. Those at 353 K only required a single kinetic model to fit the data. It is unknown whether the 353 K reactions would pass into the second regime given sufficient time but it seems likely considering the behaviour of all other reactions.

Note that in the experiments which produced mixed phases, only the Avrami parameters for the total SP have been reported given the uncertainty in partitioning the monoclinic and rhombohedral contributions to the diffraction patterns.

In all cases the initial rate of reaction (Regime 1), k, increased with increasing temperature. Differences related to composition became more apparent at the highest temperature (393 K). Na was the slowest reaction at all temperatures with K2, K3 and KNa faster and the same as each other at 353 and 368 K but with KNa slower at 393 K. K1 is slightly faster again. In Regime 2 the rates are all similar at 368 K but are again separated according to composition at 393 K with Na being the slowest followed by KNa then K1 and K3 together and K2 the fastest.

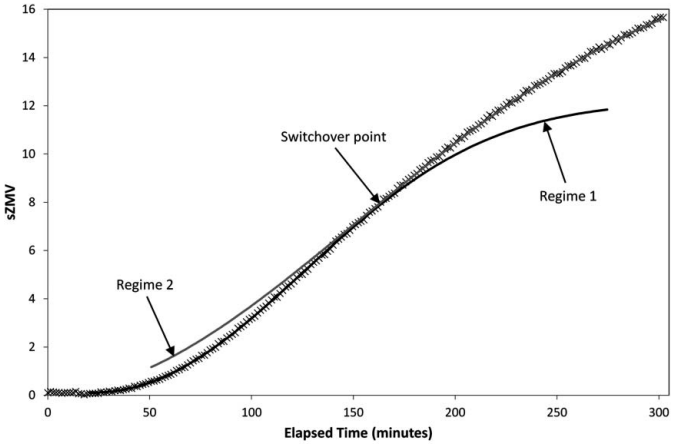

Figure 10
Plot of reaction time *versus* scaling parameter (SP) for Na at 368 K (black crosses). The calculated values from the two sequential kinetic models, designated Regime 1 (black) and Regime 2 (grey), along with the switchover point between the two are shown.

Table 4
Activation energy calculated from these *in situ* syntheses compared with literature values.

Source	Value (kJ mol^{-1})
K1 (this work)	84
K2 (this work)	91
K3 (this work)	96
KNa (this work)	92
Na (this work)	127
K (Wang *et al.*, 1985)	81
K (Kubo *et al.*, 1982)	23
K (Margulis *et al.*, 1976)	74
Na (Margulis *et al.*, 1976)	101
Na (Margulis *et al.*, 1976)	35
Na (Margulis *et al.*, 1976)	74
Na, 0 g L^{-1} seed (Dutrizac, 1996)	100
Na, 50 g L^{-1} seed (Dutrizac, 1996)	106

The rate constants calculated for Regime 1 of all reactions have been used to derive activation energies for each of the compositions *via* the Arrhenious equation [equation (6)],

$$k = A\exp(-E_a/RT), \quad (6)$$

where A is a pre-exponential factor, E_a the activation energy, R the gas constant and T the absolute temperature. Plotting $1/T$ *versus* $\ln(k)$ gives a straight line in which the y intercept is equal to $\ln(A)$ and the slope is equal to $-E_a/R$. These values are given in Table 4 and compare well with the previously reported values tabulated by Dutrizac (1996). Previous work by Dutrizac (1983) also describes a corresponding increase in rate and overall yield with temperature. This is supported by the findings in this work where the k and SP values increase with temperature (Table 3). Fig. 11 shows the increase in SP with time for the KNa series of experiments at the temperatures considered here.

The time at which the reactions change from Regime 1 to Regime 2 (the 'switch' parameter) decreases with increasing temperature. At 353 K none of the reactions ran for long enough to reach the second regime but at 368 K and 393 K the switch point was passed. At 368 K Na was by far the slowest

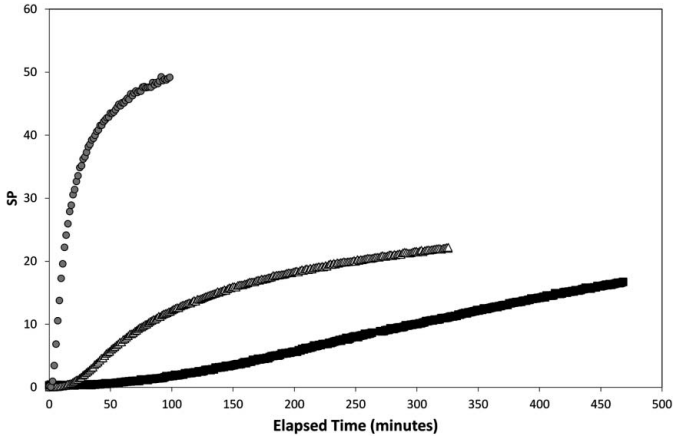

Figure 11
Plot of reaction time *versus* scaling parameter (SP) for the KNa series of reactions at 353 K (black squares), 368 K (white triangles) and 393 K (grey circles).

Table 5
Summary of values of the Avrami exponent for solid–solid interaction growth models (after Hulbert, 1969).

	Phase boundary controlled	Diffusion controlled
Three-dimensional growth		
Constant nucleation rate	4	2.5
Zero nucleation rate	3	1.5
Decreasing nucleation rate	3–4	1.5–2.5
Two-dimensional growth		
Constant nucleation rate	3	2.0
Zero nucleation rate	2	1.0
Decreasing nucleation rate	2–3	1– 2
One-dimensional growth		
Constant nucleation rate	2	1.5
Zero nucleation rate	1	0.5
Decreasing nucleation rate	1–2	0.5–1.5

(~160 min) followed by KNa, K2 and K3 at similar times (~100 min) and K1 at around 70 min. At 393 K the compositional difference was less and K1, K2 and K3 switched regimes at around 15 min while KNa and Na switched at around 30 min.

3.2.1. Avrami exponent. Ascribing physical meaning to the Avrami exponent is not a simple matter. It is related to the type of nucleation and the morphology of crystal growth but the separation of these contributions is not straightforward without additional information about the system. In the original derivation of the Avrami equation (Avrami, 1939) the exponent was held to have an integer value between 1 and 4 which reflected the nature of transformation in the solid state. A value of 4 contained contributions from a constant nucleation rate and three-dimensional growth. The value reduced with the cessation of nucleation and confinement of particles restricting dimensionality of growth. Hulbert (1969) related the value of the exponent to three categories of reaction geometry: diffusion of reactants through a product layer, nuclei growth and phase boundary reactions (*i.e.* controlled by the available interface area). A summary of these relations is given in Table 5. Relating these values directly to a solution precipitation system such as that considered here may not be entirely appropriate; however, generalizations may be made. In either a phase boundary or diffusion-controlled system reduction of the Avrami exponent corresponds to a reduction in nucleation rate and/or in the dimensionality of growth, with diffusion-controlled systems having slightly lower values. Diffusion-controlled systems are dependent upon the diffusion of reactions across a product layer. This situation is unlikely to occur in a solution precipitation system where reactants are available at the interface between the growing crystal and the solution. Such a system then is more akin to the phase boundary control scheme described for the solid state. In this case the availability of the interface area will be affected by crystallization on the vessel walls and the encroachment of neighbouring crystals.

The values of the Avrami exponent calculated for the experiments presented here show that, in general, tempera-

ture has little effect on reaction order and that the value for Regime 2 is always lower than that for Regime 1 (Table 3). This is consistent with site saturation, hindered growth and lower dimensionality of growth as the reactions progress. In the sodium series the value of the Avrami exponent for Regime 2 reduces between 368 K and 393 K. This is consistent with the overall slower reaction rate associated with the sodium compositions. For the potassium compositions there is not much change over this temperature range.

In general the parallel SAXS experiments (Brand *et al.*, 2012) suggest nucleation of quite large particles (~30 nm) prior to the detection of crystalline material in the powder diffraction runs. Optical images of the final products from both SAXS and PD experiments show, in most cases, uniform crystals (Fig. 12) suggesting that the mechanism observed in diffraction relates to the growth of pre-formed nuclei (*i.e.* zero nucleation growth). Margulis *et al.* (1976) observed that if the pH of the system was above 2 (this value decreases slightly with increased reaction temperature) the product of the reaction would be an amorphous basic sulfate. They then went on to describe the gradual conversion of this amorphous product to jarosite *via* a series of steps:

(i) Decrease in pH through the hydrolysis of Fe.

(ii) Dispersion (peptization) of amorphous basic sulfate.

(iii) Accumulation of colloidal particles with transfer of Fe from them into ionic complexes.

(iv) Accumulation of ionic complexes leading to precipitation of jarosite.

In the system considered here which commences with a neutral solution, it is feasible that an appropriate pH would be achieved to precipitate amorphous basic sulfate which would then convert to jarosite with continual lowering of the pH *via* the hydrolysis of Fe. The observation of large particles in the SAXS data prior to the observation of any crystalline material is consistent with this mechanism.

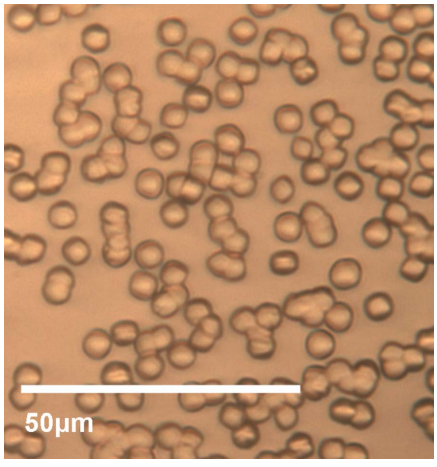

Figure 12
Optical microscope image of the final product of K1 composition formed at 353 K, from the SAXS experiment after 200 min. Note that the image has been taken through the capillary wall at room temperature approximately four days after the experiment.

4. Conclusion

In general the findings of these *in situ* experiments support the *ex situ* studies of previous work (Basciano & Peterson, 2007; Dutrizac, 1983, 1996). The effect of temperature and composition upon rate and induction period along with the calculation of activation energies is consistent with previously reported values. The presence of Na is observed to slow reaction rates even in the presence of K where the product of reaction is K-rich and more similar to K1 and K2 than Na in crystal chemistry.

The *in situ* environment provides additional information regarding the progress of reaction and intermediate states. These experiments have shown the changing kinetic behaviour of the crystallization process along with changing crystal chemistry as reactions progress. The replacement of H_3O in the *A* site with either K or Na over time is clearly evident in this dynamic data and there is also evidence for an increase in Fe content of the jarosites with time.

The high resolution of the synchrotron data has also revealed monoclinic polymorphs of jarosite which may not have been noticed using lower-resolution laboratory equipment. The ordering of the Fe vacancies with time which cause this structural distortion have also only been seen *via* the use of time-resolved methodologies. The occurrence of mixed species jarosite under varying conditions of temperature and composition has also been observed, with increasing temperature generally producing an increase in the amount of monoclinic phase formed.

The use of parallel SAXS and XRD experimentation has revealed the formation of large amorphous particles prior to crystallization. This knowledge may be exploited in the prevention of formation of detrimental jarosite films in bioleaching. Future research may focus on optimizing conditions which prevent the commencement of crystallization.

In conclusion, the use of time-resolved diffraction in this environment has shown itself to be a worthy addition to traditional *ex situ* programmes of synthesis and characterization. The results obtained *ex situ* may be replicated giving confidence in the relevance of this technique and additional information regarding kinetics and crystal chemistry may be found which would not otherwise be observed.

This research was undertaken on the powder diffraction beamline at the Australian Synchrotron, Victoria, Australia, with assistance from beamline scientist Kia Wallwork. Thanks to Ian Madsen, Robert Knott and Miao Chen for help with the syntheses and synchrotron data collections and to Alan Coelho for his assistance with the *TOPAS* protocol.

References

Avrami, M. (1939). *J. Chem. Phys.* **7**, 1103.
Basciano, L. C. (2008). Thesis. Queen's University, Canada.
Basciano, L. C. & Peterson, R. C. (2007). *Am. Mineral.* **92**, 1464–1473.
Basciano, L. C. & Peterson, R. C. (2008). *Am. Mineral.* **93**, 853–862.
Bayliss, P., Kolitsch, U., Nickel, E. H. & Pring, A. (2010). *Mineral. Mag.* **74**, 919–927.
Brand, H. E. A., Scarlett, N. V. Y. & Grey, I. E. (2012). *J. Appl. Cryst.* **45**, 535–545.

Brown, J. B. (1970). *Can. Mineral.* **10**, 696–703.
Bruker AXS (2009). *Topas V4.2: General Profile and Structure Analysis Software for Powder Diffraction Data.* Bruker AXS GmbH, Karlsruhe, Germany.
Dutrizac, J. E. (1983). *Metall. Mater. Trans. B*, **14**, 531–539.
Dutrizac, J. (1996). *Hydrometallurgy*, **42**, 293–312.
Gasharova-Garbeva, B. (2000). Thesis, Ruprecht-Karls-Universitat, Germany.
Grey, I. E., Scarlett, N. V. Y., Bordet, P. & Brand, H. E. A. (2011). *Mineral. Mag.* **75**, 2775–2791.
Hill, R. J. & Howard, C. J. (1987). *J. Appl. Cryst.* **20**, 467–474.
Hulbert, S. F. (1969). *J. Br. Ceram. Soc.* **6**, 11–20.
Jambor, J. L. (1999). *Can. Mineral.* **37**, 1323–1341.
Khanna, Y. P. & Taylor, T. J. (1988). *Polym. Eng. Sci.* **28**, 1042–1045.
Kubisz, J. (1970). *Mineral. Pol.* **1**, 45–59.
Kubo, H., Kawahara, M. & Shirane, Y. (1982). *Nippon Kogyo Kaishi*, **98**, 1257–1261.
Madsen, I. C., Scarlett, N. V. Y. & Whittington, B. I. (2005). *J. Appl. Cryst.* **38**, 927–933.
Margulis, E. V., Getskin, L. S., Zapuskalova, N. A. & Beisekeeva, L. I. (1976). *Russ. J. Inorg. Chem.* **21**, 996–999.
Nielsen, U. G., Majzlan, J. & Grey, C. P. (2008). *Chem. Mater.* **20**, 2234–2241.
Norby, P., Cahill, C., Koleda, C. & Parise, J. B. (1998). *J. Appl. Cryst.* **31**, 481–483.
Scarlett, N. V. Y., Grey, I. E. & Brand, H. E. A. (2010). *Am. Mineral.* **95**, 1590–1593.
Scarlett, N. V. Y., Madsen, I. C. & Whittington, B. I. (2008). *J. Appl. Cryst.* **41**, 572–583.
Scarlett, N. V. Y., Rowles, M. R., Wallwork, K. S. & Madsen, I. C. (2011). *J. Appl. Cryst.* **44**, 60–64.
Schmitt, B., Brönnimann, C., Eikenberry, E., Gozzo, F., Hörmann, C., Horisberger, R. & Patterson, B. (2003). *Nucl. Instrum. Methods Phys. Res. A*, **501**, 267–272.
Stephens, P. W. (1999). *J. Appl. Cryst.* **32**, 281–289.
Thompson, P., Cox, D. E. & Hastings, J. B. (1987). *J. Appl. Cryst.* **20**, 79–83.
Wallwork, K. S., Kennedy, B. J. & Wand, D. (2007). *AIP Conf. Proc.* **879**, 879–882.
Wang, Q., Ma, R. & Tan, Z. (1985). *Zinc'85: International Symposium on the Extractive Metallurgy of Zinc*, pp. 675–690. Tokyo: Mining and Metallurgical Institute of Japan.
Xu, H., Zhao, Y., Vogel, S. C., Hickmott, D. D., Daemen, L. L. & Hartl, M. A. (2010). *Phys. Chem. Miner.* **37**, 73–82.
Zeng, W., Qiu, G., Zhou, H. & Chen, M. (2011). *Hydrometallurgy*, **105**, 259–263.